Journal of Petroleum Science and Engineering 173 (2019) 1453–1463

Contents lists available at ScienceDirect

Journal of Petroleum Science and Engineering

journal homepage: www.elsevier.com/locate/petrol

Simultaneous inversion for velocity model and microseismic sources in layered anisotropic media

Guojiao Huang[a], Jing Ba[a,*], Qizhen Du[b], José M. Carcione[a,c]

[a] School of Earth Science and Engineering, Hohai University, Nanjing, 211100, China
[b] School of Geosciences, China University of Petroleum (East China), Qingdao, 266580, China
[c] Istituto Nazionale di Oceanografia e di Geofisica Sperimentale (OGS), Borgo Grotta Gigante 42c, Sgonico, Trieste I, 34010, Italy

ARTICLE INFO

Keywords:
Microseismic location
Simultaneous inversion
Layered anisotropic media
Seismic tomography

ABSTRACT

Microseismic monitoring is widely applied in fracturing operations, reservoir delineation and water front monitoring. Microseismic inversion generally uses an initial velocity model based on well logs and seismic data from perforation shots. This model is generally not suitable to locate microseismic sources. To reduce errors, we have developed a method that simultaneously updates the velocity model and locates events in space and time. 1-D layered anisotropy with a transversely-isotropic (TI) symmetry is assumed, where the symmetry axis can be arbitrarily oriented. The arrival times and ray paths of the qP, qSV and qSH waves are calculated with a modified multistage shortest path algorithm. Combined with the conjugate gradient method, a damped, minimum-norm, least-squares and constrained problem is solved. The numerical examples show that the proposed algorithm can be used to invert the anisotropic velocity model (elastic moduli and interface depth for each layer) and locate the microseismic sources and their onset times, simultaneously. It is shown that the algorithm is not very sensitive to random noise, which may be contained in arrival times and model anisotropy heterogeneities.

1. Introduction

Hydraulic fracturing is routinely performed for producing oil and gas from unconventional oil and gas reservoirs (e.g. tight oil and gas reservoirs, shale oil and gas) (Albright and Pearson, 1982; Rutledge et al., 2004; Maver et al., 2010; Maxwell et al., 2010b; Wang et al., 2016). Microseismic monitoring methods are widely used to characterize the generated fracture networks and estimate the stimulated reservoir volume. They play an important role in hydraulic fracturing analyses. However, there are two fundamental factors which may affect the accuracy of the microseismic source location. Besides the difficulty for accurately picking the first arrivals, which is specifically caused by the low signal-to-noise ratio, uncertainties in the velocity model may introduce additional errors. Generally, the velocity model is constructed with well-log data and seismic data from perforation shots (Warpinski et al., 2005; Pei et al., 2009; Maxwell et al., 2010a). However, this model is not updated when performing the location of the microseismic events. Two factors may introduce errors (Grechka, 2010). First, subsurface regions illuminated by the perforation shots are generally different from the ones covered by the microseismic events. Fracturing can take place a few hundred meters away from the perforation shots (Rutledge and Phillips, 2003). Second, hydraulic stimulation increases the pore pressure and affects the velocity model by generating fractures and cracks. Perforation data are generally collected before fracturing and a velocity model obtained with these data cannot precisely describe the temporal variations of the rock velocity field. Especially for shale rocks, fracturing may generate crack-induced azimuthal anisotropy (Tsvankin and Grechka, 2011). One important approach for solving this problem is to locate the microseismic events by inverting the velocity structure simultaneously.

In earthquake seismology, the velocity and the hypocenter parameters are usually inverted simultaneously. Aki and Lee (1976) inverted the velocity structure and hypocenter in Bear Valley, California, by using first-arrival P-wave traveltimes. Since the work of the Aki and Lee (1976), the method has been extended. It is now known as Local Earthquake Tomography (LET) (Iyer and Hirahara, 1993), which is effective in imaging subsurface structures in seismically active areas (Thurber, 1983; Zhao et al., 1992; Paul et al., 2001; Husen et al., 2003; Martakis et al., 2006; Yolsal-Çevikbilen et al., 2012; Piana Agostinetti et al., 2015; Ochoa-Chávez et al., 2016). Eberhart-Phillips (1990) used the pseudo bending method in LET instead of the approximate ray tracing method (Thurber, 1983).

The LET method has also been used in microseismic monitoring. Zhang et al. (2009) extended the double-difference tomography method

* Corresponding author.
E-mail addresses: baj04@mails.tsinghua.edu.cn, jba@hhu.edu.cn (J. Ba).

https://doi.org/10.1016/j.petrol.2018.10.071
Received 8 June 2018; Received in revised form 16 October 2018; Accepted 22 October 2018
Available online 24 October 2018
0920-4105/ © 2018 Elsevier B.V. All rights reserved.

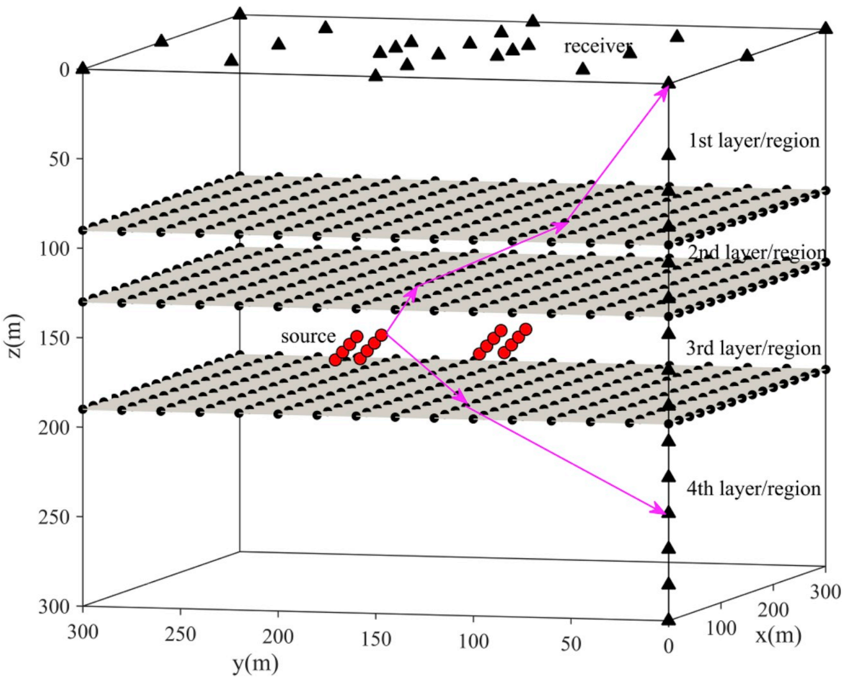

Fig. 1. Model parameterization in 1-D layered TI media. The red circles and black triangles are sources (activated fractures) and receivers, respectively, and the black circles represent nodes (interface elements). (For interpretation of the references to colour in this figure legend, the reader is referred to the Web version of this article.)

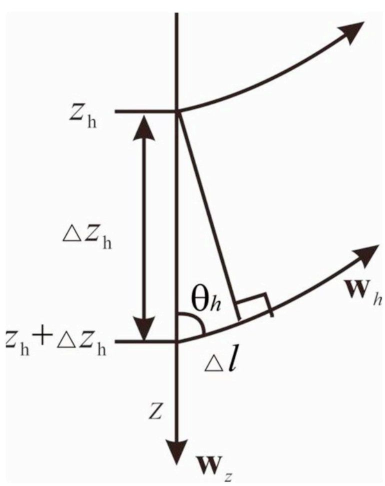

Fig. 2. A change in depth Δz_h of the hypocenter results in a perturbation on the arrival time.

(Zhang and Thurber, 2003) to locate seismic events and recover Vp, Vs and Vp/Vs models simultaneously. They used arrival times from five monitoring wells, which are rarely available. Moreover, the medium was assumed isotropic. Isotropy was also assumed by Zheng et al. (2016), who combined the time reversal imaging (TRI) method and frequency-dependent traveltime inversion (FWT) to compute the velocity model and the event locations. However, velocity model and source location were separately handled. The inverted model using FWT is applied in TRI to update the event locations, which are used in the next iteration of FWT. Li et al. (2013, 2014) developed a new method to simultaneously locate the events and perform anisotropy tomography by using differential arrival times and differential back-azimuths. The method is constrained to a 1-D layered VTI model (transversely isotropic with a vertical symmetry axis) and the origin times are not updated in the joint inversion. Grechka et al. (2011) and Grechka and Yaskevich (2013) estimated the triclinic velocity anisotropy of a medium by determining microseismic locations simultaneously. Yuan and Li (2017) performed a joint inversion for low-symmetry anisotropic media (e.g. orthorhombic anisotropy) and event locations by using S-wave splitting measurements based on a genetic algorithm. Although the medium is not VTI, it assumes that the region between the microseismic events and the receivers is homogeneous. This assumption may be unrealistic as the receiver array often spans a large depth range.

Previous studies consider relatively simple cases, such as homogeneous anisotropic media or VTI media. These models cannot accurately describe the subsurface (e.g., the azimuthal anisotropy caused by cracks), and imply significant errors in the location of the hypocenters. We consider here more realistic models, represented by layered TI media. We determine the anisotropic velocity model and the hypocenter parameters by using first-arrival qP, qSV and qSH waves in a 1-D layered TI medium (transverse isotropy with an arbitrary orientation of the symmetry axis). The model involves five density-normalized elastic moduli for each layer and the layer depth. The hypocenter parameters consist of the spatial coordinates and the origin times of the events. The method has been applied to isotropic media by Huang et al. (2012). The conjugate gradient (CG) iterative algorithm is used to solve a damped minimum-norm least-squares constrained problem. The algorithm has the following advantages (Zhou et al., 1992): (1) it considers the errors of the model and arrival times; (2) the solutions are not very sensitive to data errors; (3) it reduces the non-uniqueness of the solution by using a priori information; and (4) it uses limited computer time and memory space. Moreover, we have improved the multistage shortest path method, to calculate ray paths and arrival times, to make it suitable for a 1-D layered TI medium. We apply the method to surface and downhole microseismic surveys, and test the algorithm for its sensitivity to random noise and velocity heterogeneities.

2. The forward modeling

Computing the arrival times efficiently is an important aspect of the algorithm. Rawlinson and Sambridge (2004) proposed the multistage technique and implemented the fast marching method to perform the multiphase tracking calculation in complex layered media. Bai et al. (2009) used the improved shortest path algorithm, which is combined with multistage calculation to track multiple waves in 2-D/3-D layered media. The algorithm is also generalized to the irregular shortest path algorithm (Bai et al., 2010). The results show that the improved shortest path algorithm is superior to the fast marching method for both accuracy and CPU time (for the same model and precision, the CPU time of the fast marching method is generally five to six times that of the improved shortest path method). In our case, it is not necessary to perform a velocity parameterization of the whole model, since the elastic parameters are constant within each layer in a 1-D layered medium. We combine the method of multistage shortest path algorithm and interface element to develop a forward modeling algorithm, which is suitable for computing the microseismic ray paths and arrival times in 1-D layered TI media. In this method, the model parameterization is performed only for the layer interfaces, which can reduce the calculation time of wavefront expansion. Ray propagation nodes are interface discrete points (interface elements). The ray propagates along a straight line in the layer.

The basic principle of the modified multistage shortest path algorithm based on interface elements is implemented as follows. Firstly, the model is parameterized with a given cell size and divided into several relatively independent computational regions according to the location of the layer interfaces. Fig. 1 shows a test model divided into four layers/regions. The black circles are discrete nodes (interface elements), and the sources (red circles) and receivers (black triangles) are also nodes. Seven physical quantities are used, including five density-normalized elastic moduli (C_{11}, C_{13}, C_{33}, C_{44}, C_{66}) and two symmetry-axis angles (θ_0, ϕ_0). Alternatively, Thomsen's parameters (Thomsen, 1986) α_0 (the vertical P-wave velocity), β_0 (the vertical S-wave velocity) and the three anisotropy parameters ε, δ (orδ^*) andγ, can be used to describe the properties of the medium (weak anisotropy is not assumed). The phase velocity v_p and group velocity v_g for the qP, qSV and qSH waves can be found for instance in Zhou and Greenhalgh (2004, 2008) or in Carcione (2014):

$$v_p^{1,2} = \sqrt{P \pm \sqrt{P^2 - Q}}\,,\ \ v_p^3 = \sqrt{C_{44} + (C_{66} - C_{44})\sin^2\vartheta}\,, \tag{1}$$

where

$$\begin{aligned} P &= [C_{33} + C_{44} + (C_{11} - C_{33})\sin^2\vartheta]/2,\\ Q &= [C_{44} + (C_{11} - C_{44})\sin^2\vartheta][C_{33} + (C_{44} - C_{33})\sin^2\vartheta] - (C_{13} + C_{44})^2\\ &\quad \sin^2\vartheta\cos^2\vartheta,\\ \cos\vartheta &= \sin\theta_0\sin\theta\cos(\phi - \phi_0) + \cos\theta_0\cos\theta. \end{aligned} \tag{2}$$

$$\begin{cases} (v_g^m)_h = v_p^m\sin\vartheta + \cos\vartheta\dfrac{\partial v_p^m}{\partial\vartheta},\\ (v_g^m)_z = v_p^m\cos\vartheta - \sin\vartheta\dfrac{\partial v_p^m}{\partial\vartheta}, \end{cases} \tag{3}$$

where

$$\begin{aligned} \frac{\partial v_p^{1,2}}{\partial\vartheta} &= \frac{1}{2v_p^{1,2}}\left[\frac{\partial P}{\partial\vartheta} \pm \frac{1}{\sqrt{P^2 - Q}}\left(P\frac{\partial P}{\partial\vartheta} - 0.5\frac{\partial Q}{\partial\vartheta}\right)\right],\\ \frac{\partial v_p^3}{\partial\vartheta} &= \frac{1}{2v_p^3}[(C_{66} - C_{44})\sin 2\vartheta],\\ \frac{\partial P}{\partial\vartheta} &= 0.5(C_{11} - C_{33})\sin 2\vartheta,\\ \frac{\partial Q}{\partial\vartheta} &= [(C_{44} + (C_{11} - C_{44})\sin^2\vartheta)(C_{44} - C_{33}) + (C_{33} + (C_{44} - C_{33})\sin^2\vartheta)(C_{11} - C_{44})] \times \sin 2\vartheta - 0.5(C_{44} + C_{13})^2\sin 4\vartheta. \end{aligned} \tag{4}$$

where the superscripts 1, 2 and 3 on the left side of equation (1) and the superscripts $m = 1$, 2 and 3 in equation (3) represent the three wave modes: qP, qSV and qSH, respectively. The angle ϑ is measured from the wave direction to the symmetry axis of the medium.

The multi-stage calculation is implemented region by region from the source location. As shown in Fig. 1, the third layer containing the hypocenter is used as the first computing region, in which the minimum traveltime from the hypocenter to each node is calculated. Then, the traveltimes and corresponding ray paths on the interface elements are saved. From here, a downward or upward propagation of a transmitted wave can be simulated in the adjacent regions, starting at the interface elements with minimum arrival time. According to Huygens' Principle,

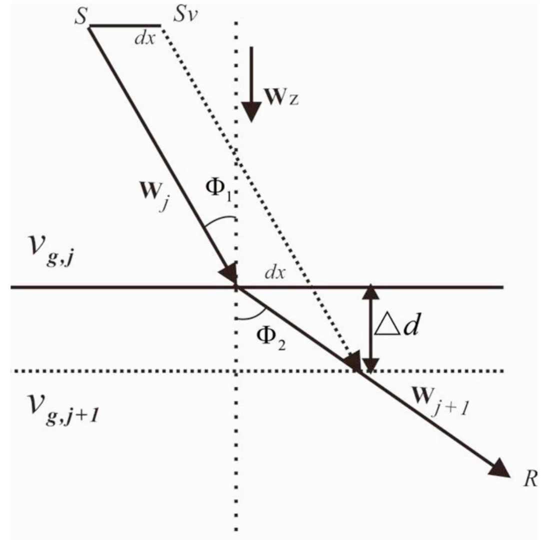

Fig. 3. Ray paths and traveltime perturbations caused by layer interface variations. S denotes the source and R denotes the receiver. The group angle and group velocity are Φ_1, $v_{g,j}$ in the first medium, and Φ_2, $v_{g,j+1}$ in the second medium, respectively. The original ray is denoted by the solid line and the perturbed interface and ray path are denoted by the dashed lines. $\mathbf{w}_j$ is a unit vector parallel to rays in layer j and $\mathbf{w}_{j+1}$ is a unit vector parallel to rays in layer $j+1$. $\mathbf{w}_z = (0,0,1)$.

the minimum arrival time node is regarded as a secondary focus on the wavefront to propagate into next region. If the minimum arrival time node is on the second interface, the upward propagation wave is calculated in the second layer. Otherwise, the downward propagation wave is calculated in the fourth layer. After the second or fourth layer is handled, we continue the calculation of a new region, and repeat until all the nodes in the model are covered. Finally, the arrival time and ray path from the hypocenter to each receiver are picked. There is no need to perform re-calculations for multiple receivers.

3. Inversion method

The CG method is used to solve the damped minimum-norm least-squares constrained problem. The objective function, and the derivatives of the arrival times with respect to the elastic moduli, layer interface depth and hypocenter locations, are derived in the next sections.

3.1. Simultaneous inversion strategy

The objective function of the damped minimum-norm least-squares constrained problem is

$$S(\mathbf{m}) = \frac{1}{2}[(\mathbf{A}\delta\mathbf{m} - \delta\mathbf{t})^T\mathbf{W}_d^{-1}(\mathbf{A}\delta\mathbf{m} - \delta\mathbf{t}) + \mu\delta\mathbf{m}^T\mathbf{W}_m^{-1}\delta\mathbf{m}],\ \mathbf{a} \le \delta\mathbf{m} \le \mathbf{b} \tag{5}$$

The first term in the right side is the arrival-time term and the second one is the regularization term. Most of previous studies

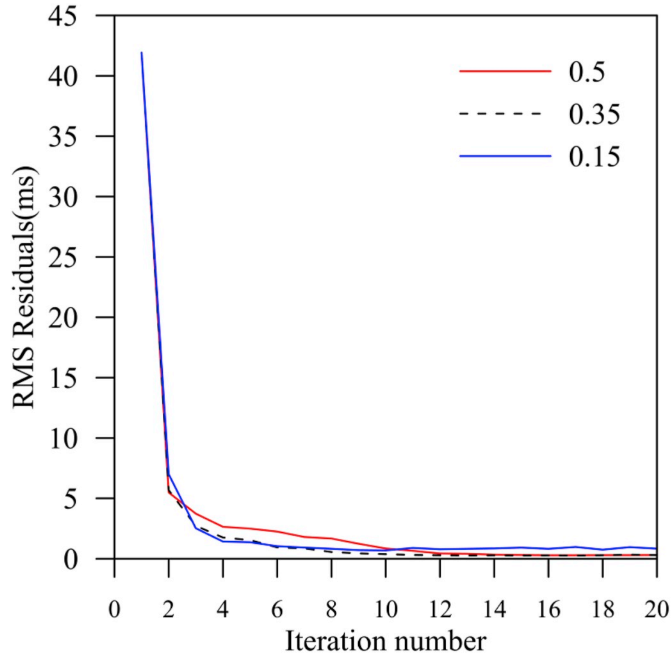

Fig. 4. The convergence curves of arrival time residuals with three different damping factors.

only included the first item (e.g. Li et al., 2013, 2014). The regularization term provides additional constraints on the model parameters and reduces the non-uniqueness of the solution. $\boldsymbol{\delta t} = [p_1(\delta t_1^1, \delta t_2^1 ......\delta t_{M_1}^1), p_2(\delta t_1^2, \delta t_2^2 ......\delta t_{M_2}^2), ..., p_n(\delta t_1^n, \delta t_2^n ......\delta t_{M_n}^n)]$ are the arrival time residuals between the observed and theoretical data. Because of the different pick accuracies, $p_1, p_2, ...p_n$ stand for the weights of the qP, qSV and qSH wave modes. n is the number of seismic phases, and $M_1, M_2, ...M_n$ are the numbers of rays corresponding to the different seismic phases. $\boldsymbol{\delta m} = [\boldsymbol{\delta C}_{ij}; \boldsymbol{\delta D}; \boldsymbol{\delta X};\ ]$ is the model perturbation related to the updated model, $\boldsymbol{\delta C}_{ij}(ij = 11,13,33,44,66)$ is the perturbation of the elastic moduli, $\boldsymbol{\delta D}$ is the perturbation of the layer interface depth, and $\boldsymbol{\delta X}$ is the perturbation of the hypocenter and origin time of events. $\mathbf{W}_d^{-1}$ and $\mathbf{W}_m^{-1}$ represent the inverse operators of the priori covariance matrices or the weighting matrices of the data and model spaces, respectively. $\mathbf{A} = \left[\frac{\partial t}{\partial m}\right]_{(M_1+M_2+...M_n)\times N}$ is the Jacobian (or Fréchet derivatives) matrix, where N is the total number of parameters to be inverted. Finally, μ is the damping factor, and $(\mathbf{a}, \mathbf{b})$ are the upper and lower values of the parameter perturbation.

The normal equation of the objective function (5) is obtained as

$$[\mu\mathbf{W}_m^{-1} + \mathbf{A}^T\mathbf{W}_d^{-1}\mathbf{A}]\boldsymbol{\delta m} = \mathbf{A}^T\mathbf{W}_d^{-1}\boldsymbol{\delta t} \tag{6}$$

The conjugate gradient method (Zhou et al., 1992) is used to solve equation (6). The determination of soft bounds (W_d, W_m) is relatively involved. The determination method can be found in Menke (1984), Tarantola (1987) and Carrion (1989). If the errors of the observed data and uncertainties in the initial model are assumed to be uncorrelated,

Table 1
Elastic moduli and corresponding Thomsen parameters.

Layer	C_{11} (km/s)^2	C_{13} (km/s)^2	C_{33} (km/s)^2	C_{44} (km/s)^2	C_{66} (km/s)^2	α_0 km/s	β_0 km/s	ε	δ^*	γ	θ_0	ϕ_0
1	20.011	7.505	16.403	5.588	7.153	4.050	2.364	0.11	0.13	0.14	45°	0°
2	22.821	8.364	18.404	6.401	7.937	4.290	2.530	0.12	0.14	0.12	45°	0°
3	18.478	6.145	13.199	5.198	7.278	3.633	2.280	0.20	0.25	0.20	45°	0°
4	23.800	8.693	19.193	7.198	8.350	4.381	2.683	0.12	0.22	0.08	45°	0°

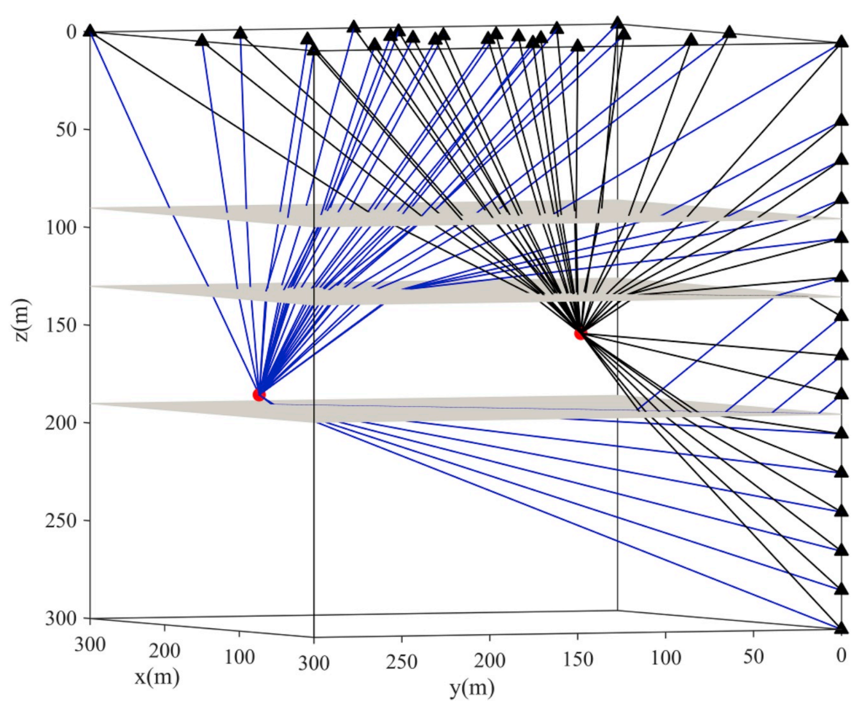

Fig. 5. The ray paths of the qP wave for the two events corresponding to the fractures.

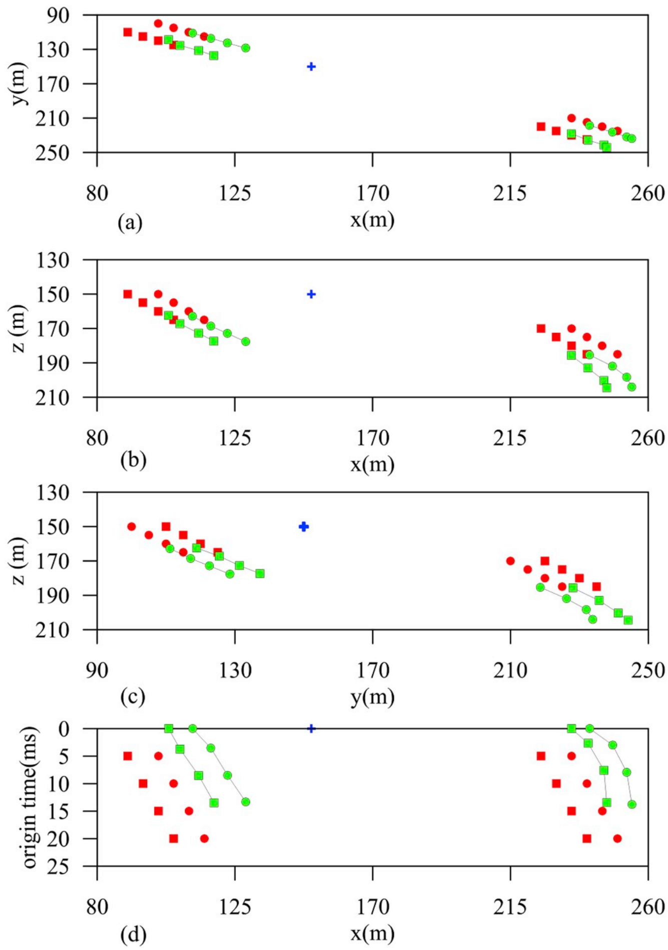

Fig. 6. Inversion with an isotropic velocity model. Panels a–c show the relocated spatial coordinates in the XY, XZ and YZ planes, respectively, and panel d shows the inverted origin times. Red dots and squares indicate the real values, and blue crosses indicate the initial values. The green dots and squares indicate the inverted values. (For interpretation of the references to colour in this figure legend, the reader is referred to the Web version of this article.)

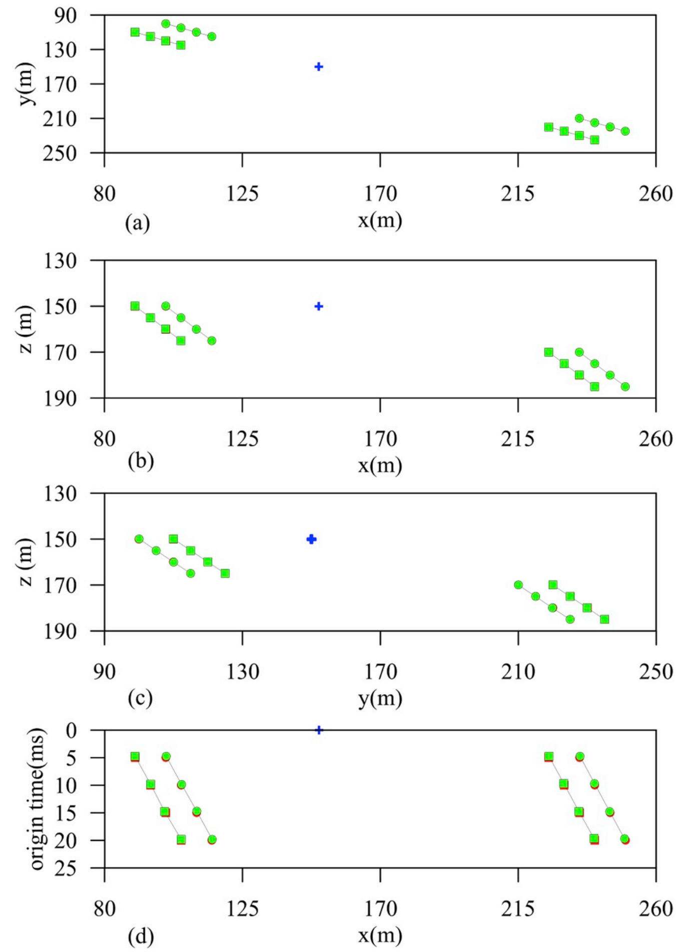

Fig. 7. Same as Fig. 6 but using an anisotropic model.

respectively, then $W_d = [\delta_{ij}(\sigma_d^j)^2]$ and $W_m = [\delta_{ij}(\sigma_m^j)^2]$, where σ_d^j is the uncertainty of the *j-th* arrival time, and σ_d^j is the uncertainty associated with the *j-th* model parameter of the initial model. Strictly speaking, W_d is best referred to as a data weighting matrix rather than a data covariance matrix unless it truly reflects the uncertainty associated with the observed data. Similarly, W_m is referred to as a model weighting matrix unless its entries reflect the true statistical uncertainties of the initial model. More accurate data or initial model parameters are given a larger weight. It can reduce the impact of data and initial model errors in the inversion solution, thus improving the accuracy. The iteration is terminated when the arrival time residuals reach a certain desired value. In order to ensure the convergence of the iterative inversion, different values for the damping factor μ are tested.

3.2. Jacobian matrix

The Jacobian matrix consists of three parts, namely the arrival-time derivative with respect to: the elastic moduli, the interface depth and the hypocenter location and origin time, i.e.

$$\Delta t = \sum_{k=1}^{N}\left(\frac{\partial t}{\partial C_{ij}^k}\right)\cdot \Delta C_{ij}^k + \sum_{k=1}^{M}\left(\frac{\partial t}{\partial d_k}\right)\cdot \Delta d_k + \sum_{k=1}^{4}\left(\frac{\partial t}{\partial x_k}\right)\cdot \Delta x_k \tag{7}$$

Here C_{ij}^k and d_k are the elastic moduli of the k-th layer and depth of the k-th layer interface, respectively, while ΔC_{ij}^k and Δd_k are the relative perturbations of C_{ij}^k and d_k, respectively. N is the number of layers that the ray intersects and M is the number of layer interfaces which are intersected by the ray. Δx_k (k = 1, 2, 3 and 4) are the relative perturbations of the hypocenter locations in the X, Y and Z directions and origin time (k = 4), respectively.

3.2.1. Sensitivity with respect to the elastic moduli

The derivative with respect to elastic moduli can be obtained from the first-order traveltime perturbation equation in terms of the phase-velocity derivatives (Zhou et al., 2008):

$$\delta t = -\int_R \frac{\delta C_{ij}}{v_p v_g}\frac{\partial v_p}{\partial C_{ij}} ds \tag{8}$$

where v_p and v_g are the phase and group velocities, respectively. The integral path R is the ray path, and ds represents the length of the ray segment within the cell after the model is parameterized. From equation (8), the derivative of the arrival time with respect to the elastic moduli C_{ij} in the k-th layer is

$$\frac{\partial t}{\partial C_{ij}^k} = -\frac{l_k}{v_{p,k} v_{g,k}}\frac{\partial v_{p,k}}{\partial C_{ij}^k} \tag{9}$$

where l_k is the ray length within the k-th layer, and $v_{p,k}$ and $v_{g,k}$ are the phase and group velocities of the k-th layer, respectively. The derivatives $\partial v_{p,k}/\partial C_{ij}^k$ can be directly obtained from equations (1) and (2) as

$$\frac{\partial v_{p,k}}{\partial C_{ij}^k} = \frac{1}{2v_{p,k}}\begin{cases}\frac{\partial P}{\partial C_{ij}^k} \pm \frac{1}{\sqrt{P^2-Q}}\left(P\frac{\partial P}{\partial C_{ij}^k} - \frac{1}{2}\frac{\partial Q}{\partial C_{ij}^k}\right), (qP,\ qSV) \\ \frac{\partial C_{44}^k}{\partial C_{ij}^k}\cos^2\vartheta + \frac{\partial C_{66}^k}{\partial C_{ij}^k}\sin^2\vartheta,\ (qSH)\end{cases} \tag{10}$$

where $v_{p,k}$ is calculated using equation (1). Moreover,

$$\frac{\partial P}{\partial C_{ij}^k} = \begin{cases}\frac{1}{2}\sin^2\vartheta, & C_{ij}^k = C_{11}^k \\ \frac{1}{2}\cos^2\vartheta, & C_{ij}^k = C_{33}^k \\ \frac{1}{2}, & C_{ij}^k = C_{44}^k \\ 0, & others\end{cases} \tag{11}$$

$$\frac{\partial Q}{\partial C_{ij}^k} = \begin{cases}\frac{C_{33}^k}{4}\sin^2 2\vartheta + C_{44}^k\sin^4\vartheta, & C_{ij}^k = C_{11}^k \\ \frac{C_{11}^k}{4}\sin^2 2\vartheta + C_{44}^k\cos^4\vartheta, & C_{ij}^k = C_{33}^k \\ C_{11}^k\sin^4\vartheta + C_{33}^k\cos^4\vartheta - \frac{C_{13}^k}{2}\sin^2 2\vartheta, & C_{ij}^k = C_{44}^k \\ -\frac{(C_{44}^k + C_{13}^k)}{2}\sin^2 2\vartheta, & C_{ij}^k = C_{13}^k \\ 0. & others\end{cases} \tag{12}$$

3.2.2. Sensitivity with respect to the hypocenter location and origin time

The partial derivative of the arrival time with respect to the origin time can be obtained from the equation $t = t_o + T$, where t is the arrival time, t_o is the origin time and T is the traveltime:

$$\frac{\partial t}{\partial t_0} = 1 \tag{13}$$

Fig. 2 illustrates how to calculate the partial derivative of the arrival time with respect to the hypocenter location using the phase velocity. If the depth of the hypocenter varies by Δz_h, the corresponding arrival time perturbation is

$$\Delta t = \frac{\Delta l}{v_{p,h}} = \frac{\Delta z_h\cos\theta_h}{v_{p,h}} = \frac{-\mathbf{w}_z\cdot\mathbf{w}_h}{v_{p,h}}\Delta z_h \tag{14}$$

where θ_h is the angle between the phase slowness vector and the z-axis at the hypocenter, $v_{p,h}$ is the phase velocity at the hypocenter, and unit vectors ($\mathbf{w}_z$ and $\mathbf{w}_h$) are displayed in Fig. 2. The first-order accurate expression for the partial derivatives is

$$\frac{\partial t}{\partial z_h} = -\frac{\mathbf{w}_z\cdot\mathbf{w}_h}{v_{p,h}} \tag{15}$$

Similarly, the partial derivatives for the other two spatial coordinates are given by

$$\frac{\partial t}{\partial x_h} = -\frac{\mathbf{w}_x\cdot\mathbf{w}_h}{v_{p,h}} \tag{16}$$

$$\frac{\partial t}{\partial y_h} = -\frac{\mathbf{w}_y\cdot\mathbf{w}_h}{v_{p,h}} \tag{17}$$

where $\mathbf{w}_x = (1,0,0)$ and $\mathbf{w}_y = (0,1,0)$ are unit vectors.

The partial derivative of the arrival time with respect to the hypocenter location is derived by using the phase velocity. The arrival time perturbation is calculated on the basis of the distance traveled by the wave in the direction of the phase slowness. Using the phase velocity instead of the group velocity in equation (15)–(17) does not introduce significant errors.

3.2.3. Sensitivity with respect to the layer interface depth

The perturbation of the ray path and arrival time caused by the change of the layer depth is displayed in Fig. 3. Obeying Snell's law, the seismic wave at the receiver R is assumed to arrive from the virtual source Sv after the interface location has changed. The arrival time perturbation at the receiver R can be decomposed into two parts: (1) Δt_1 with Δd caused by group velocity and ray path changes; (2) Δt_2 caused by moving the original source S to the virtual source location Sv. Then, the arrival time perturbation caused by the interface location variation is

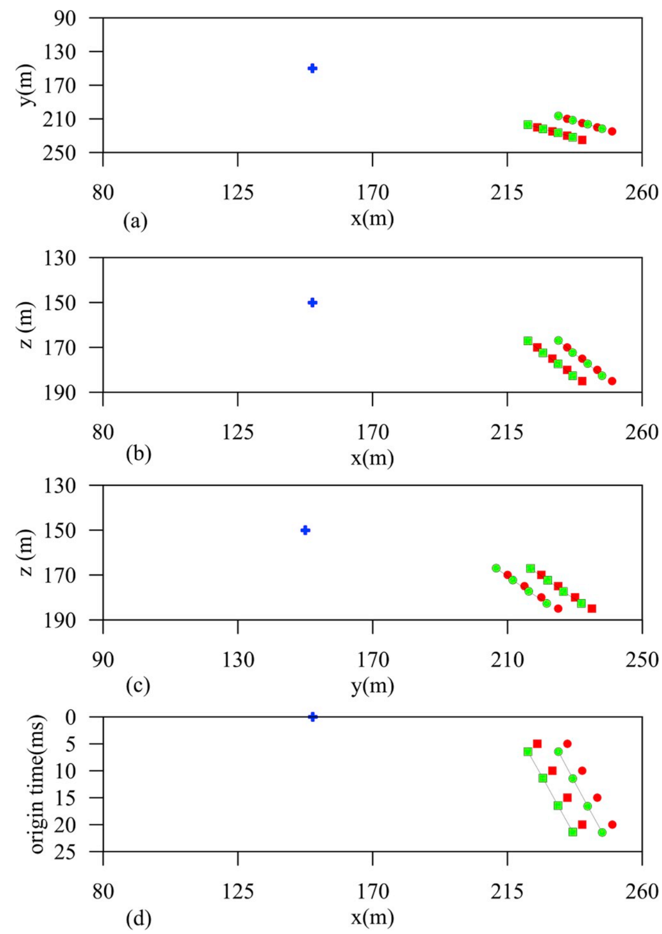

Fig. 8. Microseismic location using the arrival times of one fracture system. Panels a–c show the relocated spatial coordinates in the XY, XZ and YZ planes, respectively, and panel d is the inverted origin time. Red dots and squares indicate the real values, and blue crosses indicate the initial values. The green dots and squares indicate the inverted values. (For interpretation of the references to colour in this figure legend, the reader is referred to the Web version of this article.)

$$\begin{aligned}\Delta t = \Delta t_1 + \Delta t_2 &= \left(\frac{1}{v_{g,j}}\frac{\Delta d}{\cos\Phi_1} - \frac{1}{v_{g,j+1}}\frac{\Delta d}{\cos\Phi_2}\right) - \frac{\mathbf{w}_x\cdot\mathbf{w}_h}{v_{p,h}}dx \\ &= \frac{\Delta d}{v_{g,j}}\frac{1}{\mathbf{w_j}\cdot\mathbf{w}_z} - \frac{\Delta d}{v_{g,j+1}}\frac{1}{\mathbf{w_{j+1}}\cdot\mathbf{w}_z} - \frac{\mathbf{w}_x\cdot\mathbf{w}_h}{v_{p,h}}(\Delta d\tan\Phi_2 - \Delta d\tan\Phi_1) \\ &= \frac{\Delta d}{v_{g,j}}\frac{1}{\mathbf{w_j}\cdot\mathbf{w}_z} - \frac{\Delta d}{v_{g,j+1}}\frac{1}{\mathbf{w_{j+1}}\cdot\mathbf{w}_z} + \Delta d\frac{\mathbf{w}_x\cdot\mathbf{w}_h}{v_{p,h}}\left(\sqrt{\left(\frac{1}{\mathbf{w_j}\cdot\mathbf{w}_z}\right)^2 - 1}\right. \\ &\quad \left. - \sqrt{\left(\frac{1}{\mathbf{w_{j+1}}\cdot\mathbf{w}_z}\right)^2 - 1}\right)\end{aligned} \tag{18}$$

Then, the sensitivity with respect to the layer interface depth can be obtained as

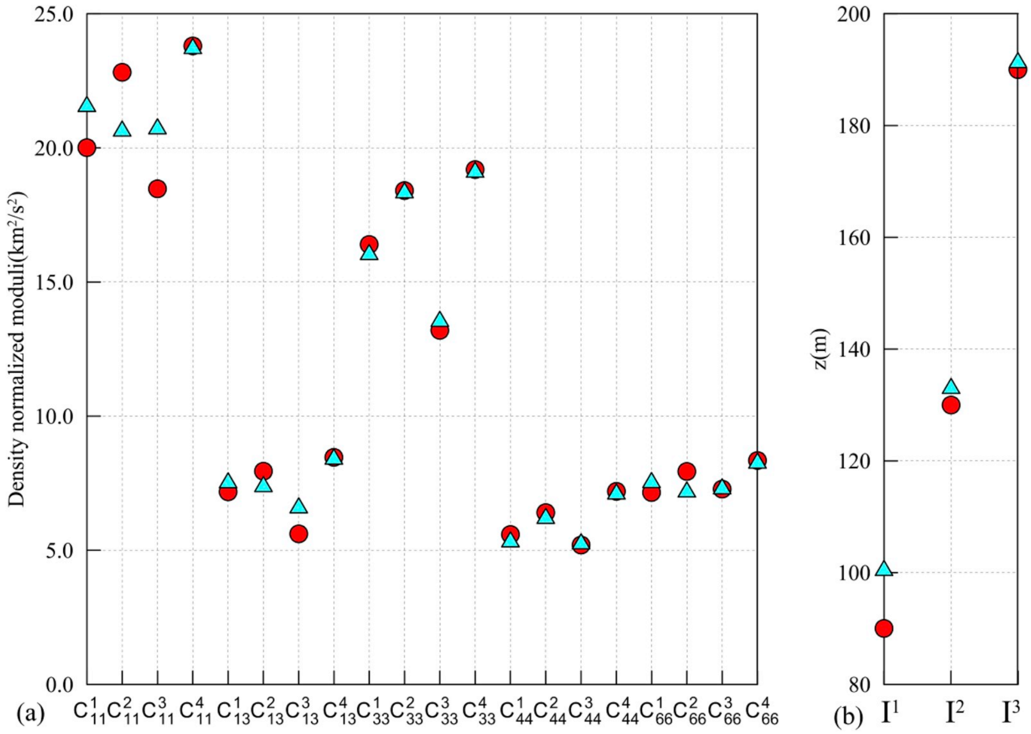

Fig. 9. Comparison between the true values of elastic moduli and layer interface depth and the inverted, using the arrival times of one fracture system. Red dots and teal triangles stand for the true parameter values and the updated values, respectively. The superscript in the elastic constants denotes the layer number. (For interpretation of the references to colour in this figure legend, the reader is referred to the Web version of this article.)

$$\frac{\partial t}{\partial d} = \frac{1}{v_{g,j}}\frac{1}{\mathbf{w_j}\cdot\mathbf{w}_z} - \frac{1}{v_{g,j+1}}\frac{1}{\mathbf{w_{j+1}}\cdot\mathbf{w}_z} + \frac{\mathbf{w}_x\cdot\mathbf{w}_h}{v_{p,h}}\left(\sqrt{\left(\frac{1}{\mathbf{w_j}\cdot\mathbf{w}_z}\right)^2-1} - \sqrt{\left(\frac{1}{\mathbf{w_{j+1}}\cdot\mathbf{w}_z}\right)^2-1}\right) \tag{19}$$

where $v_{g,j}$ and $v_{g,j+1}$ are the group velocities above and below the layer interface, respectively. $v_{p,h}$ is the phase velocity at the source S. Unit vectors ($\mathbf{w}_j$, $\mathbf{w}_{j+1}$, $\mathbf{w}_z$) are displayed in Fig. 3, and $\mathbf{w}_h$ is the slowness unit vector at the source S. Note that equation (19) is valid for any ray direction irrespective of whether the ray travels upwards or downwards, but $\mathbf{w}_j$ must always points towards the interface and $\mathbf{w}_{j+1}$ must always point away from the interface. Equation (19) is also suitable for the multilayer case. After the intersection points of the rays with the layer interfaces are determined, the sensitivity can be calculated for each layer by replacing the source and receiver positions shown above by these intersection points.

From the sensitivity equation derived above, it can be seen that the objective function has different sensitivities with respect to the elastic moduli, hypocenter location, origin time, and interface depth. The latter is the less sensitive parameter. There are differences in the behavior of the derivatives with respect to the elastic moduli for each wave mode (equation (10)), which vary as a function of the wavefront direction (equations (11) and (12)). The derivatives with respect to the source coordinates or the layer interface depth are related to the ray path and wavefront direction (equations (15)–(17), (19)). In summary, the sensitivities are related to the angle of the ray; therefore, the inversion result is depending on the ray coverage.

4. Numerical experiments and discussion

In order to illustrate the performance of the proposed inversion algorithm, we select a 3-D TI model to simultaneously invert the velocity model (elastic moduli and layer interface depths) and the microseismic parameters (spatial locations and origin times). Zhou and Greenhalgh (2008) mentioned that it is difficult to obtain reasonable solutions when the angles defining the symmetry axis (θ_0, ϕ_0) are free parameters. This is because (θ_0, ϕ_0) are highly sensitive to the phase velocity and arrival times. We assume that these angles are known and that the only unknowns at each node are the five elastic moduli. The arrival times of the qP, qSV and qSH waves are calculated by the improved shortest path algorithm introduced in Section 2. According to the theory, the weighting matrices $\mathbf{W}_d^{-1}$ and $\mathbf{W}_m^{-1}$ in equation (6) should be derived from a priori information of the data noise and model parameter variations (Menke, 1984; Tarantola, 1987; Carrion, 1989) to reduce multiple solutions. Here, we assign unit operators to the weighting matrices $\mathbf{W}_d^{-1} = \mathbf{I}_d$ and $\mathbf{W}_m^{-1} = \mathbf{I}_m$, which means that no a priori information is available. The pick accuracies of the three wave modes are assumed to be the same, that is $p_1 = p_2 ..... = p_n = 1$. Through several trial calculations, the optimal damping factor μ is determined according to the convergence of the arrival-time residuals. Here we select the root-mean square (RMS) of the arrival time residuals as the measure of convergence of the arrival time residuals between the observed and computed arrival times for each loop of the iteration. As an example, Fig. 4 gives the convergence of the residuals when the three different damping factors (μ = 0.5, 0.35, 0.15) are selected in the simultaneous inversion with one fracturing system. It can be seen that the damping factor μ= 0.35 is the best.

As shown in Fig. 1, a 3-D TI model is selected for the numerical experiments. This model has a size of 300 m × 300 m × 300 m, four layers and three layer interfaces at 90, 130 and 190 m. The elastic moduli and the corresponding Thomsen parameters are shown in Table 1. A grid size of 10 m × 10 m × 10 m is used to parameterize the layer interfaces. There are 24 geophones distributed on the upper surface and 14 geophones in the borehole (see Fig. 1 for details) to simulate surface and downhole microseismic observations. Two fracture systems are shown in Fig. 1. Each system is made of two neighboring parallel fractures and each fracture is associated with four events. The origin times of each fracture are 5 ms, 10 ms, 15 ms and 20 ms.

The arrival times of the three wave modes (direct qP, qSV and qSH waves) are used in the inversion. Fig. 5 shows the ray paths of the qP waves for the two events corresponding to the fractures in Fig. 1. It is shown that the ray-angle coverages in different layers differ. The third layer is has the lowest velocity and pseudo-refracted seismic waves occurs at the second and third interfaces.

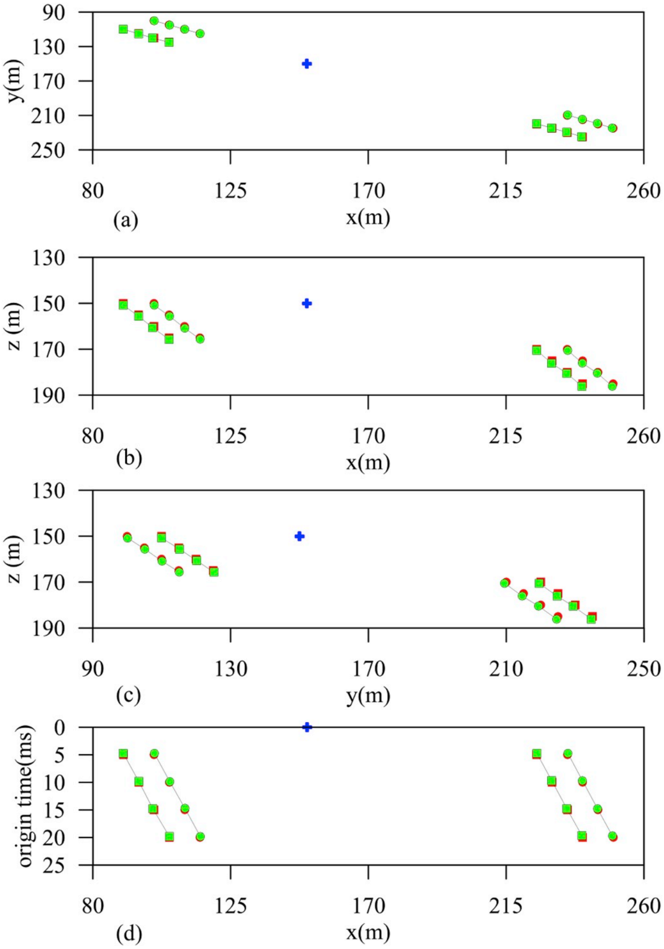

Fig. 10. Same as Fig. 8 but with the two fracture systems.

The influence of seismic anisotropy on the microseismic location is investigated by comparing the inversions assuming isotropy and anisotropy. In the isotropy inversion, accurate P-wave velocity models are obtained on the basis of the perforation shots. For the anisotropy inversion, we use sixteen microseismic events under ideal free-noise conditions. The initial value of the microseismic location is (150, 150, 150) m, and the starting origin time is 0 ms. Figs. 6 and 7 show the isotropy and anisotropy result, respectively. It is shown that the isotropic results greatly differ from the true values, including the absolute (or relative) locations and origin times of the sixteen events. The anisotropy inversion gives better results. Even in the case that the difference between the initial source parameters and true values is large, the inverted source positions (Fig. 7a–c) and origin time (Fig. 7d) agree well with the true values.

The algorithm requires the simultaneous inversion of the velocity model and event location. The initial (or starting) model is as follows: The elastic parameters of the first layer are the initial values of the elastic parameters of each layer; the difference between the initial layer interface depth and the correct value is 10 m; the initial spatial coordinates and origin times of the sixteen events are the same, (150, 150, 150) m and 0 ms, respectively.

Two different sets of microseismic events were selected to test the ability of the inversion algorithm under different ray coverages. The first set makes use of the first arrivals of the qP, qSV and qSH waves from one fracture system. The inversion results are shown in Fig. 8 (microseismic location results) and 9 (the inverted anisotropic velocity model). From the location results (Fig. 8), it can be seen that the event positions are recovered in relative terms, e.g., the fracture is successfully delineated, showing a clear parallel structure, but differs in location compared to the correct one. The inversion of the five elastic parameters in Fig. 9 differs. For example, the results for C_{44} and C_{66} are better than those of the other three elastic parameters, and very close to the true values (see Fig. 9a). This is because, despite the same ray coverage, the sensitivity of the different parameters is not the same (equations (9)–(12)). This difference is mainly caused by the fact that the derivative of the phase velocity with respect to different parameters is different. It is determined by the properties of the anisotropic medium, since different elastic parameters have different contributions to the phase velocity. Even for the same elastic parameter, the sensitivity changes with the ray angle, so that the elastic moduli of the second layer with different ray-angle coverage (see Fig. 5) may be recovered relatively well. However, the elastic parameters of the first and second layers are not well inverted (Fig. 9a) if the depth of the first-layer interface is poorly updated (see Fig. 9b).

The second set of events is based on the first arrivals of the qP, qSV

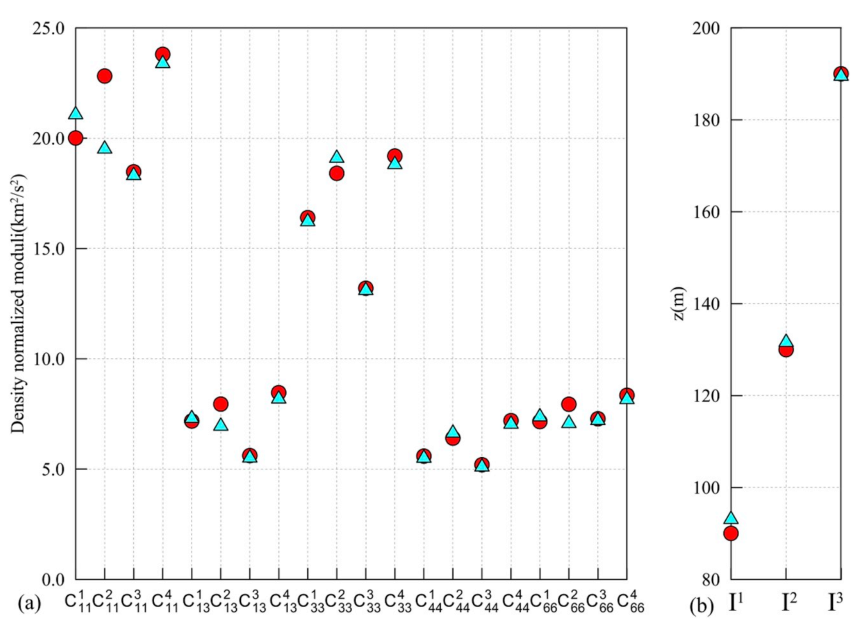

Fig. 11. Same as Fig. 9 but with the two fracture systems.

Table 2
Differences between the true values of elastic parameters and layer interface depth and the inverted results with or without random noise. DC_{11}, DC_{13}, DC_{33}, DC_{44} and DC_{66} are the elastic parameter error; DD respects the layer interface depth error.

Layer	DC_{11}(km/s)^2		DC_{13}(km/s)^2		DC_{33}(km/s)^2		DC_{44}(km/s)^2		DC_{66}(km/s)^2		DD(m)	
	no noise	noise	no noise	noise	no noise	noise	no noise	noise	no noise	noise	no noise	noise
1	1.16	0.74	0.21	0.05	0.09	0.06	0.01	0.02	0.26	0.32	3.52	12.12
2	3.21	2.85	0.90	0.89	0.79	0.79	0.33	0.45	0.65	0.76	2.05	0.38
3	0.07	0.51	0.01	0.21	0.00	0.00	0.00	0.00	0.02	0.07	0.03	0.07
4	0.32	0.60	0.18	0.18	0.29	0.09	0.02	0.06	0.09	0.12	–	–

Table 3
Differences between the true values of hypocenter parameters and the inverted results with or without random noise. DX, DY and DZ are the coordinate error; DT respects the error of the origin time.

Source number	DX(m)		DY(m)		DZ(m)		DT(ms)	
	no noise	noise	no noise	noise	no noise	noise	no noise	noise
1	0.06	0.18	0.03	0.01	0.79	0.74	0.28	0.28
2	0.02	1.64	0.17	0.56	0.63	1.01	0.16	0.40
3	0.40	0.77	0.19	1.28	0.33	0.67	0.23	0.28
4	0.01	1.23	0.14	0.69	0.70	0.15	0.04	0.18
5	0.11	0.00	0.11	0.46	0.09	0.82	0.17	0.25
6	0.12	0.14	0.13	0.28	0.67	0.70	0.01	0.15
7	0.08	1.09	0.08	1.67	0.85	0.35	0.28	0.10
8	0.10	0.70	0.11	0.23	0.65	0.56	0.18	0.21
9	0.04	0.40	0.46	1.28	0.52	1.09	0.25	0.49
10	0.13	0.09	0.24	1.12	0.55	1.10	0.17	0.32
11	0.18	0.01	0.57	0.89	0.48	0.72	0.22	0.08
12	0.25	0.91	0.27	0.45	1.12	0.82	0.32	0.31
13	0.14	0.45	0.47	2.88	0.51	0.09	0.28	0.04
14	0.08	0.71	0.39	2.53	1.06	0.22	0.31	0.38
15	0.16	1.88	0.61	1.49	0.47	0.19	0.22	0.44
16	0.31	1.59	0.38	2.35	1.11	3.42	0.30	0.55
average	0.14	0.74	0.27	1.14	0.66	0.79	0.21	0.28

and qSH waves of the two fracture systems. The inversion results are shown in Fig. 10 (microseismic location) and 11 (inverted anisotropic velocity model). By comparing Fig. 11 with Fig. 9, it is evident that when only one fracture system is used, the inversion of the velocity model yields results which differ from the correct values. When using the two fracture systems, both the elastic parameters and interface depths are improved and converge to the true values, except for C_{11}^2 and C_{33}^2. This is because the depth of the layer interface and elastic moduli for each layer are biased to some degree. When two hydraulic fracturing systems are used, the inverted first layer interface depth is significantly improved, and the accuracy of the inverted elastic moduli (here C_{11}^2 and C_{33}^2) slightly decreases. In summary, when the velocity model inversion is improved, the accuracy of the corresponding microseismic-event locations are also improved (Fig. 10). Therefore, when the ray-angle coverage is good, a microseismic location with simultaneous anisotropic velocity structure tomography is feasible.

The ray-angle coverage is always related to the number and arrangement of the receivers. Here the receivers are located on the surface and in a single well, positioned at random to ensure a good coverage of the ray angle. In addition to the receiver arrangement, the number of receivers also affects the inversion results. If this number is too small, the inversion is undetermined; if it is too large, the economic cost is too high. It was found that as the receivers increase, the

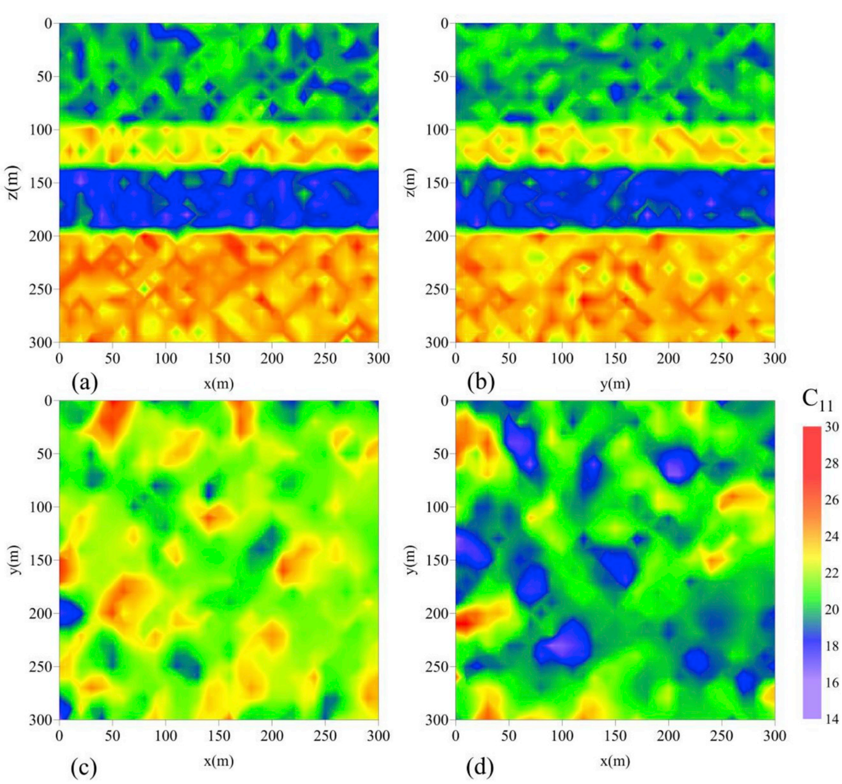

Fig. 12. Randomly perturbed model for C_{11}(km^2·s^{-2}). Plot (a) and (b) are the XZ plane at y = 0 and YZ plane at x = 50 m, respectively. Plot (c) and (d) are the XY plane at z = 100 m and z = 160 m, respectively.

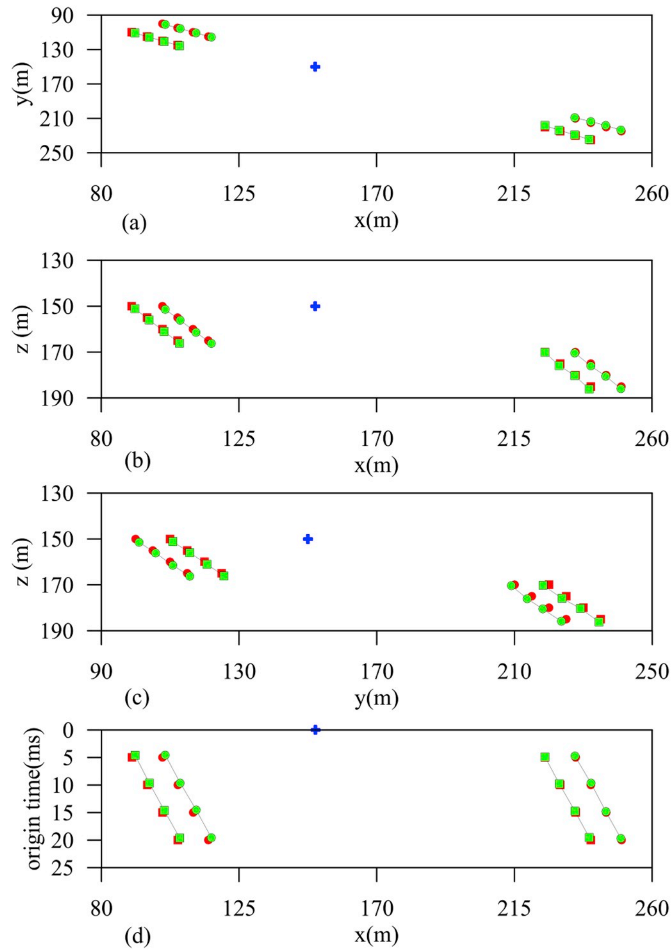

Fig. 13. Microseismic location results by using the random perturbed velocity model. Red dots and squares indicate the real values, and blue crosses indicate the initial values. The green dots and squares indicate the inverted values. (For interpretation of the references to colour in this figure legend, the reader is referred to the Web version of this article.)

inversion error decreases; but when the number of receiver increases to a certain amount, the inversion error tends to be constant. In these examples, we have considered 40 receivers as the best choice.

To investigate the effects of first-arrival pick uncertainties, 5% random noise are added to the arrival times of the qP, qSV and qSH waves. The noise-free and noise-containing inversion error is displayed in Tables 2 and 3. Comparing the results before and after the addition of random noise, it is shown that the precision decreases in the presence of noise, especially the first layer interface depth (Table 2). After adding random noise, the average location error in the X, Y and Z directions increase to about 1 m, which is acceptable. Therefore, the effect of random noise in this case is not very important, and the model parameters still converge quite well to the true values.

Next, we test the sensitivity of the method in the presence of heterogeneities by using the anisotropic TI model shown in Fig. 12. The heterogeneities are added as a strong random perturbation of the layered TI model used in the previous examples. The random perturbations are applied to the five elastic moduli (C_{11}, C_{13}, C_{33}, C_{44}, C_{66}), with a maximum of 15%, i.e.

$$C_{ij}(x, y, z) = C^0_{ij}(x, y, z) + 0.15R\cdot C^0_{ij}(x, y, z) \tag{20}$$

where R denotes a random number. The observed arrival times take into account the perturbations but the model is approximated with the uniform 1-D layered TI model. The initial values of the inversion parameters are the same of the last test, where we have introduced noise. Fig. 13 shows the results. The events locations differ slightly from the true locations, especially at depth (Fig. 13c). The relative locations are recovered relatively well. Fig. 14 gives the velocity model results. The elastic moduli in each layer and the respective layer depths are recovered with different degrees of precision.

5. Conclusions

In order to reduce the effects of velocity-model uncertainties on the location of microseismic events, we present an inversion algorithm for simultaneous inversion of the model and event location, based on a 1-D layered TI medium with arbitrary symmetry axis orientations. The improved shortest path algorithm is used to calculate the ray paths and arrival times of the first arrivals. The partial derivatives with respect to the elastic moduli, layer interface depths, spatial coordinates and origin

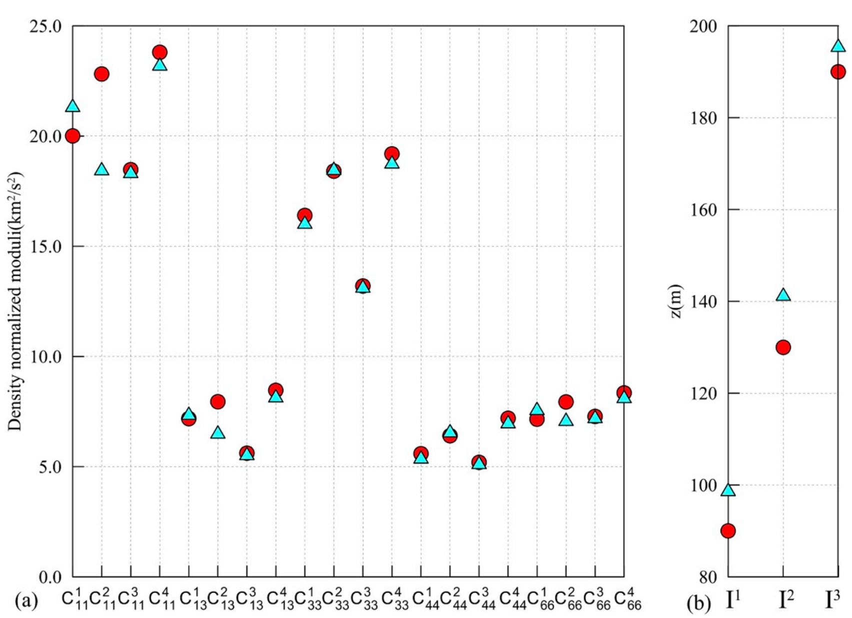

Fig. 14. Comparisons between the true values of the elastic moduli and layer interface depths with the inverted results. Red dots and light-blue triangles indicate the true and computed values, respectively. The superscript in the elastic constants denotes the layer number. (For interpretation of the references to colour in this figure legend, the reader is referred to the Web version of this article.)

times of the microseismic events are re-derived here for this anisotropic velocity model. The conjugate gradient algorithm is used to solve the constrained damped least-squares problem. Then, a method is developed to simultaneously invert the anisotropic velocity model (elastic moduli and layer interface depths) and hypocenter parameters (spatial locations and origin times). The numerical simulation results by using surface and downhole microseismic data show that the algorithm can effectively perform the inversion with good ray coverage. The results are not very sensitive to relative low random noise and velocity heterogeneities which may affect the arrival times and the velocity model. However, the method has been applied to synthetic data. For actual production, the ray coverage may not be good due to sparse distribution of microseismic events and geophones. In future studies, it is necessary to test the reliability and robustness of the method with real data.

Acknowledgements

This research work was supported by the National Natural Science Foundation of China (41504038); the Natural Science Foundation of Jiangsu Province (BK20150799); the Fundamental Research Funds for the Central Universities (2017B12014); the Distinguished Professor Program of Jiangsu Province, China and the State Key Laboratory of Earthquake Dynamics Open Funds (LED2017B01).

Appendix A. Supplementary data

Supplementary data to this article can be found online at https://doi.org/10.1016/j.petrol.2018.10.071.

References

Aki, K., Lee, W.H.K., 1976. Determination of the three–dimensional velocity anomalies under a seismic array using first P arrival times from local earthquakes: 1.A homogeneous initial model. J. Geophys. Res. 81, 4381–4399.

Albright, J.N., Pearson, C.F., 1982. Acoustic emissions as a tool for hydraulic fracture location: experience at the Fenton Hill hot dry rock site. Soc. Petrol. Eng. J. 22 (4), 523–530.

Bai, C.Y., Tang, X.P., Zhao, R., 2009. 2D/3D multiply transmitted, converted and reflected arrivals in complex layered media with the modified shortest path method. Geophys. J. Int. 179, 201–214.

Bai, C.Y., Huang, G.J., Zhao, R., 2010. 2D/3D irregular shortest-path raytracing for multiple arrivals and its applications. Geophys. J. Int. 183, 1596–1612.

Carrion, P.M., 1989. Generalized non-linear elastic inversion with constraints in model and data spaces. Geophys. J. Int. 96, 151–162.

Carcione, J.M., 2014. In: Wave Fields in Real Media. Theory and Numerical Simulation of Wave Propagation in Anisotropic, Anelastic, Porous and Electromagnetic Media, third ed. Elsevier extended and revised).

Eberhart-Phillips, D., 1990. Three-dimensional P and S velocity structure in the coalinga region, California. J. Geophys. Res. 95, 15343–15363.

Grechka, V., 2010. Data-acquisition design for microseismic monitoring. Lead. Edge 29, 278–282.

Grechka, V., Singh, P., Das, I., 2011. Estimation of effective anisotropy simultaneously with locations of microseismic events. Geophysics 76, WC141–WC153.

Grechka, V., Yaskevich, S., 2013. Inversion of microseismic data for triclinic velocity models. Geophys. Prospect. 61, 1159–1170.

Huang, G.J., Bai, C.Y., Zhu, D.L., Greenhalgh, S., 2012. 2D/3D seismic simultaneous inversion for the velocity and interface geometry using multiple classes of arrivals. Bull. Seismol. Soc. Am. 102 (2), 790–801.

Husen, S., Quintero, R., Kissling, E., Hacker, B., 2003. Subduction-zone structure and magmatic processes beneath Costa Rica constrained by local earthquake tomography and petrological modelling. Geophys. J. Int. 155 (1), 11–32.

Iyer, H.M., Hirahara, K., 1993. Seismic Tomography, Theory and Practice. Chapman and Hall, London.

Li, J., Zhang, H., Rodi, W.J., Toksoz, M.N., 2013. Joint microseismic location and anisotropic tomography using differential arrival times and differential backazimuths. Geophys. J. Int. 195, 1917–1931.

Li, J., Li, C., Morton, S.A., Dohmen, T., Katahara, K., Toksoz, M.N., 2014. Microseismic joint location and anisotropic velocity inversion for hydraulic fracturing in a tight Bakken reservoir. Geophysics 79, C111–C122.

Martakis, N., Kapotas, S., Tselentis, G.-A., 2006. Integrated passive seismic acquisition and methodology: case studies. Geophys. Prospect. 54, 1–19.

Maver, K.G., Maxwell, S., Koutsabeloulis, N., Greenaway, R., 2010. The application of microseismics in the oil and gas industry. Geo ExPro 7 (4), 58–63.

Maxwell, S.C., Bennett, L., Jones, M., Walsh, J., 2010a. In: Anisotropic Velocity Modeling for Microseismic Processing: Part 1 — Impact of Velocity Model Uncertainty: 80th Annual International Meeting. SEG, pp. 2130–2134 Expanded Abstracts.

Maxwell, S.C., Rutledge, J., Jones, R., Fehler, M., 2010b. Petroleum reservoir characterization using downhole microseismic monitoring. Geophysics 75 (5) 75A129–75A137.

Menke, W., 1984. Geophysical Data Analysis: Discrete Inverse Theory. Academic Press Inc., San Diego, California, pp. 40–126.

Ochoa-Chávez, J.A., Escudero, Christian R., Núñez-Cornú, Francisco J., Bandy, William L., 2016. P-wave velocity tomography from local earthquakes in western Mexico. Pure Appl. Geophys. 173, 3487–3511.

Paul, A., Cattaneo, M., Thouvenot, F., Spallarossa, D., Béthoux, N., Fréchet, J., 2001. A three-dimensional crustal velocity model of the southwestern Alps from local earthquake tomography. J. Geophys. Res. 106 (B9), 19367–19389.

Pei, D., Quirein, J.A., Cornish, B.E., Quinn, D., Warpinski, N.R., 2009. Velocity calibration for microseismic monitoring: a very fast simulated annealing (VFSA) approach for joint-objective optimization. Geophysics 74, WCB47–WCB55.

Piana Agostinetti, N., Giacomuzzi, G., Malinverno, A., 2015. Local three-dimensional earthquake tomography by trans-dimensional Monte Carlo sampling. Geophys. J. Int. 201 (3), 1598–1617.

Rawlinson, N., Sambridge, M., 2004. Multiple reflection and transmission phases in complex layered media using a multistage fast marching method. Geophysics 69, 1338–1350.

Rutledge, J.T., Phillips, W.S., Mayerhofer, M.J., 2004. Faulting induced by forced fluid injection and fluid flow forced by faulting: an interpretation of hydraulic-fracture microseismicity, carthage cotton valley gas field, Texas. Bull. Seismol. Soc. Am. 94 (5), 1817–1830.

Rutledge, J.T., Phillips, W.S., 2003. Hydraulic stimulation of natural fractures as revealed by induced microearthquakes, Carthage Cotton Valley gas field, east Texas. Geophysics 68, 441–452.

Tarantola, A., 1987. Inverse Problem Theory, Methods for Data Fitting and Model Parameter Estimation. Elsevier, Amsterdam.

Thomsen, L., 1986. Weak elastic anisotropy. Geophysics 51, 1954–1966.

Thurber, C.H., 1983. Earthquake locations and three-dimensional crustal structure in the Coyote Lake area, central California. J. Geophys. Res. 88, 8226–8236.

Tsvankin, I., Grechka, V., 2011. Seismology of Azimuthally Anisotropic Media and Seismic Fracture Characterization. SEG.

Wang, H., Li, M., Shang, X., 2016. Current developments on micro-seismic data processing. J. Nat. Gas Sci. Eng. 32, 521–537.

Warpinski, N.R., Sullivan, R.B., Uhl, J.E., Waltman, C.K., Machovoe, S.R., 2005. Improved microseismic fracture mapping using perforation timing measurements for velocity calibration. In: Proceedings of the SPE Annual Technical Conference and Exhibition, 2003 October 5–8. Society of Petroleum Engineers, Denver, Colorado Paper 84488.

Yolsal-Çevikbilen, S., Biryol, C.B., Beck, S., Zandt, G., Taymaz, T., Adıyaman, H.E., Özaçar, A.A., 2012. 3-D crustal structure along the North Anatolian Fault Zone in north-central Anatolia revealed by local earthquake tomography. Geophys. J. Int. 188 (3), 819–849.

Yuan, D., Li, A., 2017. Joint inversion for effective anisotropic velocity model and event locations using S-wave splitting measurements from downhole microseismic data. Geophysics 82, C133–C143.

Zhang, H., Thurber, C.H., 2003. Double-difference tomography: the method and its application to the Hayward fault, California. Bull. Seismol. Soc. Am. 93, 1875–1889.

Zhang, H., Sarkar, S., Toksöz, M.N., Kuleli, H.S., Al-Kindy, F., 2009. Passive seismic tomography using induced seismicity at a petroleum field in Oman. Geophysics 74, WCB57–WCB69.

Zhao, D., Hasegawa, A., Horiuchi, S., 1992. Tomographic imaging of P and S wave velocity structure beneath Northeastern Japan. J. Geophys. Res. 97, 19909–19928.

Zheng, Y.K., Wang, Y.B., Chang, X., 2016. Wave equation based microseismic source location and velocity inversion. Phys. Earth Planet. In. 261, 46–53.

Zhou, B., Greenhalgh, S.A., Sinadinovski, C., 1992. Iterative algorithm for thedamped minimum norm, least-squares and constrained problem in seismic tomography. Explor. Geophys. 23, 497–505.

Zhou, B., Greenhalgh, S.A., 2004. On the computation of elastic wave group velocities for a general anisotropic medium. Journal of Geophysics and. Engineering 1, 205–215.

Zhou, B., Greenhalgh, S.A., Green, A., 2008. Nonlinear traveltime inversion scheme for crosshole seismic tomography in titled transversly isotropic media. Geophysics 73, D17–D33.

Zhou, B., Greenhalgh, S.A., 2008. Nonlinear traveltime inversion for 3D seismic tomography in strongly anisotropic media. Geophys. J. Int. 172, 383–394.